ISPRS Journal of Photogrammetry and Remote Sensing 216 (2024) 185–199

Contents lists available at ScienceDirect

ISPRS Journal of Photogrammetry and Remote Sensing

journal homepage: www.elsevier.com/locate/isprsjprs

Beyond clouds: Seamless flood mapping using Harmonized Landsat and Sentinel-2 time series imagery and water occurrence data

Zhiwei Li [a,b], Shaofen Xu [a], Qihao Weng [a,b,c,*]

[a] Department of Land Surveying and Geo-Informatics, The Hong Kong Polytechnic University, Hung Hom, Hong Kong
[b] Research Centre for Artificial Intelligence in Geomatics, The Hong Kong Polytechnic University, Hung Hom, Hong Kong
[c] Research Institute for Land and Space, The Hong Kong Polytechnic University, Hung Hom, Hong Kong

ARTICLE INFO

Keywords:
Flood mapping
Water body extraction
Cloud removal
HLS imagery
Cloudy and rainy environments
Time series

ABSTRACT

Floods are among the most devastating natural disasters, posing significant risks to life, property, and infrastructure globally. Earth observation satellites provide data for continuous and extensive flood monitoring, yet limitations exist in the spatial completeness of monitoring using optical images due to cloud cover. Recent studies have developed gap-filling methods for reconstructing cloud-covered areas in water maps. However, these methods are not tailored for and validated in cloudy and rainy flooding scenarios with rapid water extent changes and limited clear-sky observations, leaving room for further improvements. This study investigated and developed a novel reconstruction method for time series flood extent mapping, supporting spatially seamless monitoring of flood extents. The proposed method first identified surface water from time series images using a fine-tuned large foundation model. Then, the cloud-covered areas in the water maps were reconstructed, adhering to the introduced submaximal stability assumption, on the basis of the prior water occurrence data in the Global Surface Water dataset. The reconstructed time series water maps were refined through spatiotemporal Markov random field modeling for the final delineation of flooding areas. The effectiveness of the proposed method was evaluated with Harmonized Landsat and Sentinel-2 datasets under varying cloud cover conditions, enabling seamless flood mapping at 2–3-day frequency and 30 m resolution. Experiments at four global sites confirmed the superiority of the proposed method. It achieved higher reconstruction accuracy with average F1-scores of 0.931 during floods and 0.903 before/after floods, outperforming the typical gap-filling method with average F1-scores of 0.871 and 0.772, respectively. Additionally, the maximum flood extent maps and flood duration maps, which were composed on the basis of the reconstructed water maps, were more accurate than those using the original cloud-contaminated water maps. The benefits of synthetic aperture radar images (e.g., Sentinel-1) for enhancing flood mapping under cloud cover conditions were also discussed. The method proposed in this paper provided an effective way for flood monitoring in cloudy and rainy scenarios, supporting emergency response and disaster management. The code and datasets used in this study have been made available online (https://github.com/dr-lizhiwei/SeamlessFloodMapper).

1. Introduction

As one of the most devastating natural disasters, floods exacerbated by global climate change pose significant risks to life, property, and infrastructure globally (Rentschler et al., 2022; IPCC, 2023). Recent estimates suggest that the proportion of the global population affected by floods has increased by 20–24 % since the turn of the century, with projections indicating that up to 758 million people will be exposed to a 100-year flood event by 2030 (Tellman et al., 2021). Enhanced flood monitoring techniques, specifically focusing on near-real-time flood extent mapping, are critically important for effective emergency response and flood disaster management, to deal with the growing threat of flood disasters efficiently.

Satellite remote sensing offers a cost-effective means for continuous and extensive flood monitoring. Optical and synthetic aperture radar (SAR) images, the primary data sources in satellite-based flood monitoring, serve distinct roles given their unique characteristics. On the one hand, SAR data have generally been widely used in flood monitoring

* Corresponding author at: JC STEM Lab of Earth Observations, Department of Land Surveying and Geo-Informatics, The Hong Kong Polytechnic University, Hung Hom, Hong Kong.
E-mail address: qihao.weng@polyu.edu.hk (Q. Weng).

https://doi.org/10.1016/j.isprsjprs.2024.07.022
Received 2 February 2024; Received in revised form 19 July 2024; Accepted 25 July 2024

because of their independence from weather conditions and time of imaging. However, because of the limitations of SAR imaging mechanisms, flood monitoring with SAR data in urban areas is relatively constrained (Notti et al., 2018; Liang and Liu, 2020; McCormack et al., 2022). Additionally, the publicly available sources of SAR data are relatively limited, and the use of single-source SAR data for flood monitoring is restricted by the revisit intervals of satellites. For example, the combined Sentinel-1A/1B satellites provide SAR data with a temporal resolution of 6 days, which makes capturing short-term flood events, lasting less than 6 days, challenging. Such a situation became even worse due to the operational failure of Sentinel-1B in December 2021, which led to the temporal resolution of Sentinel-1 being reduced to 12 days. On the other hand, numerous optical satellites, such as Landsat and Sentinel-2, can provide open-access images for surface information extraction and flood mapping. However, they are inevitably affected by cloud cover, leading to the missing ground surface information in images and reducing the frequency of valid observations (Yang et al., 2020; Zeng et al., 2020; Goffi et al., 2020; Li et al., 2022c; Shastry et al., 2023). In consideration of the revisit cycles of satellites and the duration of floods with their respective intervals, the frequency of satellite observation is crucial for flood monitoring (Tulbure et al., 2022).

Flood extent mapping with satellite imagery: Mapping the extent of flood inundated areas using remotely sensed satellite imagery relies on water extraction. Existing water extraction and flood extent mapping methods primarily consist of water index- and machine learning-based methods. Water indexes, such as the normalized difference water index (NDWI) (McFeeters, 1996), modified NDWI (Xu, 2005), and automated water extraction index (Feyisa et al., 2014), are widely used to separate surface water from other ground objects because they are easy to use and computationally efficient. Traditional machine learning methods, such as support vector machines (Li and Narayanan, 2003; Sun et al., 2014, 2015) and random forest (Deng et al., 2017; Wang et al., 2018), are more effective in water extraction than index-based methods. However, they require manual extraction of spectral and spatial features, impacting prediction accuracy. The recent introduction of deep learning techniques, such as convolutional neural networks (CNN), a subset of machine learning methods, has revolutionized this field and significantly enhanced the accuracy of water extraction owing to their strong feature representation ability (Wang et al., 2020; Konapala et al., 2021; Bentivoglio et al., 2022; He et al., 2024; Valman et al., 2024). Despite the development of numerous water extraction and flood mapping methods, the negative influence of cloud cover was often avoided in previous studies only by using cloud-free optical imagery for flood monitoring (Benoudjit and Guida, 2019). Alternatively, only cloud-free optical satellite images were used to interpret land cover types before and during flood events for flood impact assessments (Huang and Jin, 2020; Psomiadis et al., 2020). Therefore, exploring the potential of using optical satellite imagery that might be cloud-covered in flood mapping to improve flood monitoring frequency is worth further investigation (DeVries et al., 2020; Li et al., 2022b). Developing a cloud reconstruction method for multisensor optical satellite imagery in cloudy scenarios is essential for seamless flood extent mapping at high temporal density.

Cloud removal for seamless flood mapping: Seamless water mapping with cloudy optical images is key for continuous flood extent mapping. Existing methods can achieve cloud removal by integrating complementary information from neighboring temporal images into the cloud-covered areas of target images after transformations (Shen et al., 2015; Zhang et al., 2021; Li et al., 2024). However, accurately reconstructing the spatial details of ground surfaces in cloud-covered areas, especially in images with land cover changes, such as flooding, is challenging. A cloud removal method for optical satellite images, targeting the application scenarios for flood monitoring, is particularly necessary to leverage multisensor satellite images for flood monitoring fully. In this case, gap-filling methods for the reconstruction of cloud-contaminated water areas, including methods based on ancillary data (e.g., inundation frequency) (Zhao and Gao, 2018; Mullen et al., 2021), spatiotemporal neighborhood similarity (Li et al., 2021; Bai et al., 2022; Huang et al., 2023), and spatiotemporal modeling (Li et al., 2022a; Bai et al., 2023), have been studied recently. Although these recent studies have developed gap-filling methods for seamless water mapping, such methods are not tailored for and validated in flooding scenarios, leaving room for further improvements. First, existing studies of index-based water extraction methods require manual feature extraction and threshold determination for water segmentation, which shows both sensitivity and limitations in accuracy. In contrast, deep learning methods, particularly recent large foundation models such as RVSA (Wang et al., 2023), RemoteCLIP (Liu et al., 2023), and Prithvi-100M (Jakubik et al., 2023), have significantly enhanced image processing accuracy and offered potential for more precise water extraction. Second, existing gap-filling methods can effectively reconstruct permanent or seasonal surface water bodies covered by clouds (Mullen et al., 2021; Bai et al., 2022; Huang et al., 2023). However, they fall short in flooding scenarios with significant surface water changes, and their performance is limited by the number of valid images during the flooding periods. Third, water occurrence data generated based on historical satellite observations show large uncertainties at low occurrence values and often ignore low-frequency water dynamics like floods. This oversight and the lack of confidence-level consideration in water occurrence make it a big challenge for a direct application of existing methods (Zhao and Gao, 2018; Li et al., 2021) for seamless flood mapping. Additionally, locally adaptive threshold determination for water segmentation based on water occurrence data warrants further consideration for accurate reconstruction under complex cloudy and rainy weather conditions. In practical flood extent mapping, the ability to obtain near-real-time inundation maps is crucial for an effective emergency response to flood disasters (Notti et al., 2018; DeVries et al., 2020; Tulbure et al., 2022). In this context, ensuring the spatiotemporal consistency of time series flood mapping results obtained based on multisensor satellite data and improving the precision of dynamic flood monitoring are additional issues to be considered.

To overcome these limitations in flood extent mapping with optical images under varying cloud cover conditions, this study introduces a robust seamless time series flood extent mapping method. This method fine-tunes a large foundation model to achieve high-precision water extraction, enables the reconstruction of cloud-covered flooding areas in optical satellite time series imagery, and conducts time series refinement via spatiotemporal modeling to improve the spatiotemporal consistency of water maps. We utilize Harmonized Landsat and Sentinel-2 (HLS) datasets (Claverie et al., 2018), which have been proven promising for high-temporal-density flood mapping (Tulbure et al., 2022), as our experimental data. HLS datasets, which harmonize images captured by the Landsat-8/9 and Sentinel-2A/B satellites, offer image time series typically at 2–3 day intervals with 30 m resolution. Through the validation of our developed seamless flood extent mapping method under varying conditions at four global sites, this study aims to answer whether cloud-covered flooding areas can be effectively reconstructed in HLS image time series. The key contributions of this study are summarized as follows:

1) We investigate the feasibility of reconstructing cloud-contaminated flooding areas by introducing a method that facilitates spatially continuous flood monitoring with cloudy time series imagery. Utilizing this approach, we can generate a time series of seamless flood extent maps, significantly mitigating the impacts of clouds on flood mapping. Additionally, we demonstrate the potential of this reconstruction method for seamless time series flood mapping by quantitatively evaluating its effectiveness under varying cloud cover conditions and at different phases of flood events. The evaluation results affirm the superiority of the proposed method in various scenarios.

2) The advantages of combining Landsat and Sentinel-2 images for flood mapping are confirmed. The benefits of further integrating SAR images (e.g., Sentinel-1) to augment flood mapping are also discussed,

which we consider a promising new paradigm for extensive application in this field.

By leveraging a combined time series of Landsat and Sentinel-2 images, this study aims to enhance the completeness, frequency, and precision of flood extent mapping in cloudy and rainy conditions, thereby improving emergency response and contributing to effective flood management.

The remaining contents are organized as follows. Section 2 introduces the proposed method and provides the implementation details. The experimental data and results are described in Section 3. In Section 4, we highlight the benefits of cloud reconstruction for flood mapping and the incorporation of SAR images for enhanced flooding area reconstruction, and then discuss the efficiency and limitations of the proposed method. Our conclusions are drawn in Section 5.

2. Methodology

This study proposes to achieve seamless flood extent mapping at 30 m resolution based on HLS imagery to improve the completeness, frequency, and precision of flood extent mapping, especially in cloud-prone areas, and to benefit flood emergency response and management. The flowchart of the proposed method is illustrated in Fig. 1. Three main steps are involved. Specifically, in order to achieve optimal performance, we first fine-tuned a large foundation model to enable accurate identification of water extents from HLS images. Then, auxiliary water occurrence data from the Global Surface Water (GSW) dataset (Pekel et al., 2016) were utilized to reconstruct cloud- and cloud-shadow-covered areas in the time series water maps based on the introduced submaximal stability assumption. The cloud/shadow mask used was defined by the Quality Assessment (QA) band included in the HLS dataset, which was generated using the Fmask algorithm (Zhu et al., 2015). Lastly, we conducted spatiotemporal modeling to minimize potential errors in water extraction and cloud reconstruction, consequently enhancing the spatiotemporal consistency of time series water maps and ensuring more accurate identification of flood extents.

2.1. Water extraction via a fine-tuned large foundation model

In this step, we harnessed the potential of a state-of-the-art deep learning model for water extraction. Specifically, we utilized the large foundation model Prithvi-100M (Jakubik et al., 2023) as the baseline, which was constructed via the temporal Vision Transformer (ViT) (Dosovitskiy et al., 2021) and pre-trained with a vast amount of harmonized Landsat-8/9 and Sentinel-2 images in HLS datasets by the NASA and IBM team (Jakubik et al., 2023). HLS datasets encompassed global coverage and yielded 30 m surface reflectance products. The baseline foundation model, pre-trained with HLS images from the contiguous United States, served as an effective feature extractor and was extended for water extraction in Landsat-8/9 and Sentinel-2 images included in HLS datasets. Highly accurate water maps are expected to be obtained by fine-tuning the foundation model with existing labeled water and flood datasets featuring Landsat and Sentinel-2 images.

The Prithvi-100M model adopted a self-supervised encoder based on ViT and employed a learning strategy involving the masked autoencoder (MAE) (He et al., 2022). It utilized the mean squared error loss function to guide model training. Operating on 3D patch data, the model was allowed to receive the input data comprising multi-temporal images. For each batch of data, the Query-Key-Value attention mechanism was introduced, enabling the model to capture both temporal and spatial features (Vaswani et al., 2017). The images used for model training comprised six bands: blue, green, red, narrow NIR, SWIR 1, and SWIR 2. This study concentrated on the task of flood segmentation for a mono-temporal image, utilizing the Prithvi-100M–Sen1Floods11 model architecture (Jakubik et al., 2023). This architecture was pre-trained on the Sen1Floods11 dataset (Bonafilia et al., 2020) for flood mapping. The model architecture is illustrated in Fig. 2. Starting with a multispectral HLS image of dimensions M × N, the model normalized the six required bands based on their corresponding mean value and variance of images in the training dataset, and performed operations such as cropping and flattening. In the encoding phase, the ViT encoder was utilized to encode the data, generating patch embeddings with positional encoding. These embeddings underwent multiple convolutions for feature extraction, and the shape of the embeddings was then transformed back to the original image size. In the decoding phase, a fully convolutional network (FCN), applying the binary cross entropy loss function, was used to implement the identification of flood-specific pixels.

To achieve optimal performance in water extraction, we fine-tuned the pre-trained Prithvi-100M–Sen1Floods11 model. During the

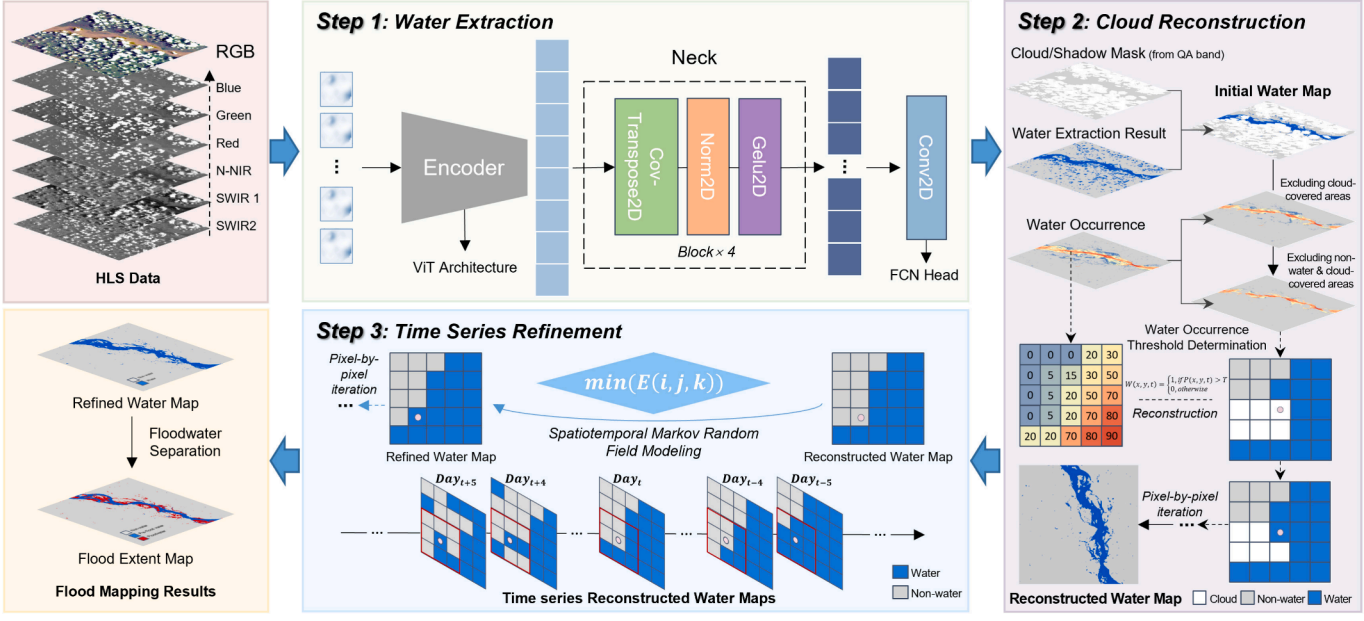

Fig. 1. Flowchart of the proposed seamless time series flood extent mapping method. Three main steps. Step 1: water extraction for each HLS image via a fine-tuned large foundation model; Step 2: reconstruction of cloud- and cloud-shadow-covered areas, as defined by the QA band of the HLS image, in each water map; and Step 3: refining time series water maps via the spatiotemporal Markov random field (MRF) modeling.

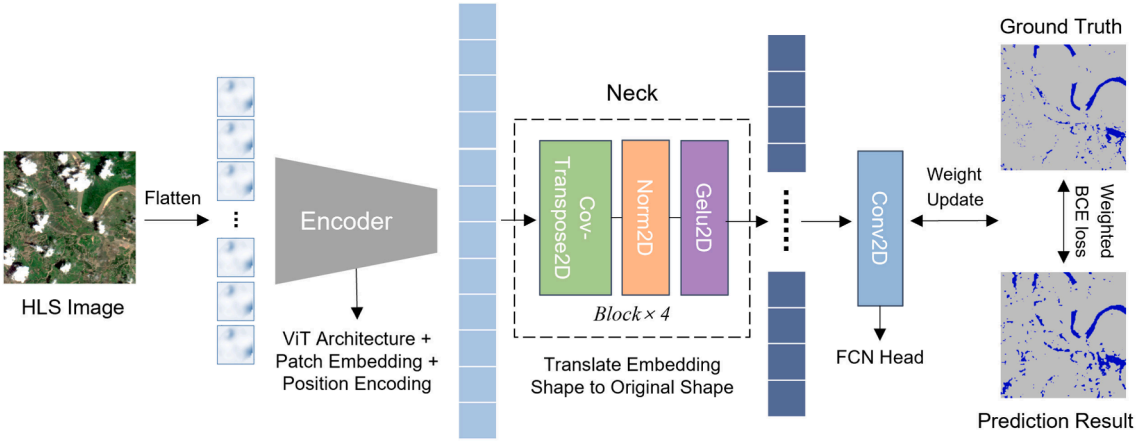

Fig. 2. The architecture of the Prithvi-100M–Sen1Floods11 model for flood mapping (Adapted from Jakubik et al., 2023).

process, we monitored the fine-tuning and evaluated the model's performance to determine the optimal model. Consequently, we selected the model with the highest overall accuracy on the Sen1Floods11 test dataset as the final model for subsequent water extraction. With the fine-tuned model, time series water maps could be obtained on the basis of the harmonized Landsat-8/9 and Sentinel-2 images. Cloud-covered areas in these images, including the clouds and the cloud shadows labeled in the quality assessment (QA) band of the HLS products, were also labeled in the time series water maps.

2.2. Reconstructing cloud-covered areas in time series water maps

To reconstruct cloud-covered areas in time series water maps, we introduced an approach that leveraged the water occurrence data included in the GSW dataset (Pekel et al., 2016). The water occurrence data, in which each pixel denotes the frequency of water presence, were crafted by aggregating monthly water coverage data using historical Landsat imagery spanning from 1984 to 2021. The assumption is that in a local area, if most cloud-free pixels possessing a certain water occurrence value are identified as water, adjacent cloud-contaminated pixels with water occurrence exceeding this value are likely to be water (Zhao and Gao, 2018; Mullen et al., 2021). This assumption strengthens as the proximity between cloud-free and cloud-contaminated pixels increases.

In addition, considering the biases inherent in the water occurrence data, to determine optimal water occurrence thresholds with high confidence automatically for the robust reconstruction of cloud-contaminated pixels under varying cloud cover conditions and water dynamics, we introduced a "***submaximal stability***" assumption. This assumption was based on our observations, which guided the threshold determination. The three observations are as follows: 1) water extents under regular conditions usually fall within the range of maximum water extents; 2) water dynamics often occur in areas with low water occurrence; and 3) random cloud cover has a greater impact on the occurrence calculation for surface water with lower occurrence than those for surface water with higher occurrence, thus indicating a trend in which low water occurrence implies low confidence. From these observations, the greatest overlap between regular and maximum water extents occurs in areas with high occurrence. Furthermore, the ratio of pixel counts in histogram bins for water occurrence within regular and maximum extents generally tends to increase across the occurrence range and can generally indicate the confidence level of water occurrence. Therefore, optimal water occurrence thresholds exceeding certain confidence levels can be determined on the basis of this generally increasing ratio and robust trend for the reconstruction of cloud-contaminated water pixels.

Consequently, we implemented the reconstruction of cloud-covered areas in time-series water maps over a local sliding window, iteratively in a pixel-by-pixel and image-by-image manner. All cloud-contaminated pixels were assigned a new class: 1 for water or 0 for non-water. The reconstruction process was applied only to cloud-contaminated pixels in the water maps, while the identified water and non-water pixels remained unchanged. The reconstructed binary water maps $W(x,y,t)$ can be formalized as follows:

$$W(x,y,t) = \begin{cases} 1, \text{if } P(x,y,t) > T \\ 0, \text{otherwise} \end{cases}, \quad (1)$$

where $P(x,y,t)$ denotes the water occurrence of pixel (x,y) at date t. T is the determined water occurrence threshold over the sliding local window centered around the target pixel.

The local window size was adaptively determined based on the cloud cover conditions within the window. To ensure that enough valid pixels were involved for reconstruction, the initial window size was set at 50 × 50 and was stepwise increased if the cloud-free pixels within the window were not predominantly water. If the window size reached the maximum height or width of the image, it was reset to the entire image size. Fig. 3 illustrates the detailed steps for the reconstruction of cloud-covered areas in an example water map. The determination of the water occurrence threshold T, which was based on the introduced "submaximal stability" assumption, involved three steps. First, the histogram of water occurrence excluding cloud-covered areas shown in Fig. 3(d) and the histogram of water occurrence excluding non-water and cloud-covered areas shown in Fig. 3(e) were computed. Then, the pixel count ratio, which is defined as the ratio of the pixel count in the histogram bin of Fig. 3(e) to that of Fig. 3(d), was obtained. This ratio indicates the proportion of observed water occurrence pixel count to the actual water occurrence pixel count and can reflect the confidence level of the water occurrence. The introduced "submaximal stability" assumption was also applicable to the water occurrence excluding cloud-covered areas in Fig. 3(e) and Fig. 3(d) because of the random distribution of clouds in images. Finally, the water occurrence threshold T was determined as the water occurrence corresponding to the first histogram bin in the range of [0,100], in which the pixel count ratio equaled or exceeded the optimal threshold of 0.35. The optimal pixel count ratio threshold was carefully selected by parameter sensitivity analysis, in which iterative tests were conducted for the pixel count ratio threshold within a typical range of [0, 0.6] at an interval of 0.01. The optimal threshold was determined on the basis of the reconstruction accuracy assessments through a series of simulation experiments, as described in Section 3.3.2. Once the water occurrence threshold within the local window was determined, if the water occurrence value of a cloud-contaminated target pixel exceeded this threshold, then the pixel was classified as water; otherwise, it was

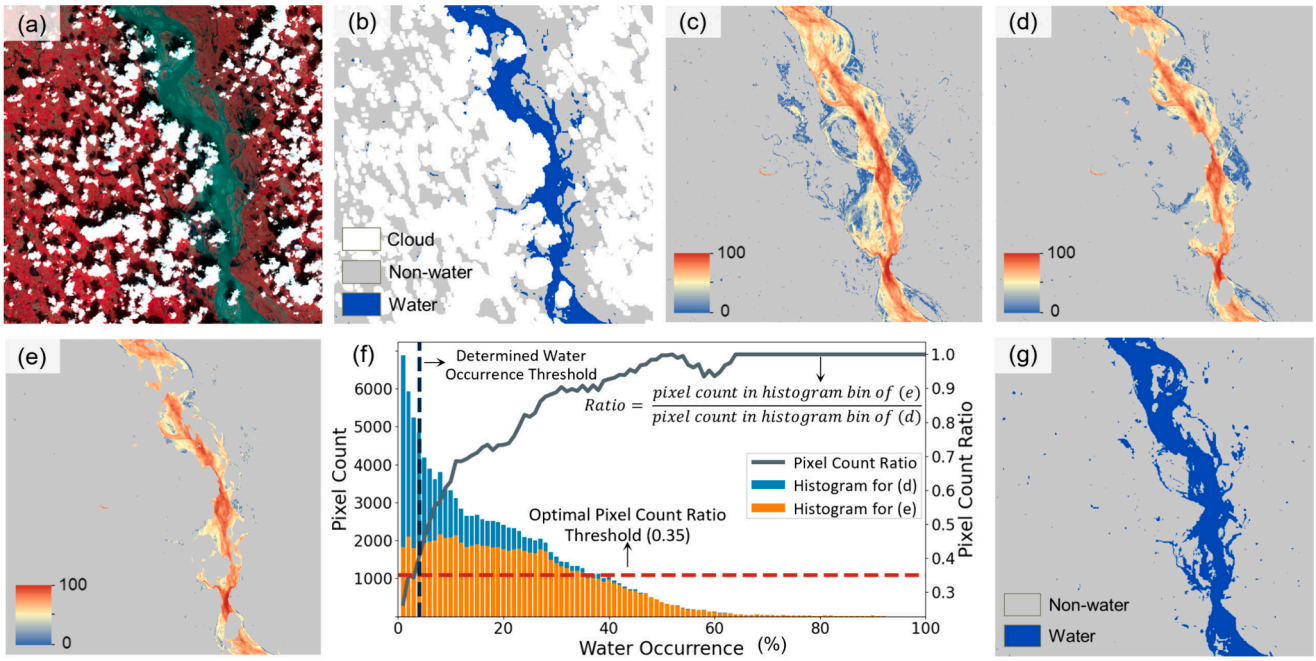

Fig. 3. Illustration of reconstruction of cloud-covered areas in the water map. (a) Cloudy HLS image; (b) Initial cloud-covered water map; (c) Water occurrence in the GSW dataset; (d) Water occurrence excluding cloud-covered areas labeled in (b); (e) Water occurrence excluding non-water and cloud-covered areas labeled in (b); (f) Water occurrence histograms for (d) and (e) and determination of the water occurrence threshold. The threshold is determined as the water occurrence corresponding to the first histogram bin in the range of [0,100], in which the pixel count ratio equals or exceeds the optimal threshold of 0.35; (g) Reconstructed binary water map.

classified as non-water, as shown in Fig. 3(g). This process continued until all cloud-covered pixels in each cloud-covered water map were reconstructed.

The proposed reconstruction approach offered two primary advantages: 1) It used locally adaptive window sizes that accounted for the spatial proximity between local areas, enhancing the accuracy and detail of reconstruction—especially beneficial for small water bodies. It also accommodated the heterogeneity in flooding area changes across different regions, including events such as dam breaches, in which the surface water in reservoirs may shrink instead of expanding like flooded areas. 2) The method employed the pixel count ratio to determine the water occurrence threshold on the basis of the introduced "submaximal stability" assumption, which offered greater stability compared with using direct pixel counts. This stability ensured that variations in the water occurrence histogram, which may arise from differing cloud cover conditions and water dynamics, leading to variable pixel counts, do not affect the threshold determination.

2.3. Time series refinement of water maps via spatiotemporal MRF modeling

Inconsistencies may exist in reconstructed time series water maps owing to differences among images captured under varying cloud cover conditions. In this study, spatiotemporal MRF modeling was employed to refine the reconstructed time series water maps and enhance their spatiotemporal consistency. Specifically, each pixel in time series water maps belonged to only two possible classes, i.e., water and non-water, denoted as 1 and 0, respectively. Given that water areas are likely to be connected patches and that the water body at a given pixel is likely to persist for certain periods even during flood events, the time series water maps were assumed to satisfy the MRF properties with a Gibbs potential function in spatial and temporal domains (Moussouris, 1974; Li, 2009; Kasetkasem et al., 2014). The Gibbs potential function defined the energy of a configuration, i.e., the sum of the potential (or cost) for spatial and temporal local neighborhoods. Thus, a spatiotemporal MRF model was constructed to minimize an energy function to find the most likely state configuration, indicating the classes of water and non-water for each pixel. The energy function $E(i,j,k)$ for a given target pixel at location (i,j) and date k can be formalized as follows:

$$E(i,j,k) = \sum_{s\in S}\sum_{t\in T} w_{s,t}\cdot I\left(x_{s,t} \neq x_{i,j,k}\right), \tag{2}$$

where $I(\text{Å}\cdot)$ checks whether the class of pixels in spatial ($s \in S$) and temporal ($t \in T$) neighborhoods is different from the center pixel $x_{i,j,k}$. The weight $w_{s,t}$ is determined on the basis of spatiotemporal proximity to the center pixel, in which a smaller spatiotemporal proximity leads to a larger weight, defined as follows:

$$w_{s,t} = \gamma \frac{\frac{1}{D_s}}{\sum_{s\in S}\frac{1}{D_s}} + \beta \frac{\frac{1}{D_t}}{\sum_{t\in T}\frac{1}{D_t}}, \tag{3}$$

where γ and β are the balanced parameters applied to the spatial and temporal terms, respectively. D_s is the 2D Euclidean distance from the pixel in neighborhood S to the center pixel $x_{i,j,k}$. D_t refers to the temporal distance from the pixel in adjacent timeslots T to the target date k. In this study, the size of neighborhood S is empirically set to 3 × 3 pixels to preserve spatial detail efficiently; the time range of adjacent timeslots T is set to be $[k-5, k+5]$, which ensures that only timely information is involved during reconstruction, considering the typical duration of flood events.

A smaller weight of 0.75 was specifically assigned to the reconstructed pixel compared with that for the clear pixel during the energy computation process to mitigate the uncertainty in refinement due to potential reconstruction errors. The optimal classes (i.e., water and non-water) were assigned to each pixel in the reconstructed time series water maps, determined by achieving the minimum energy state calculated using Equations (2) and (3). Refined time series water maps were generated by applying the refinement process to each pixel accordingly.

Flood inundated areas were identified by excluding pre-flood water from the refined time series water maps. In this study, the maximum water extent prior to a flood was determined from the time series water

maps. Water within this extent was labeled as pre-flood water on the flood extent map, while water outside this extent was labeled as flood-water. Consequently, three classes, namely, non-water, pre-flood water, and flood water, were labeled on the final time series flood extent maps.

3. Results and analysis

3.1. Experimental data

In this study, four global study sites located in four different countries were selected. The geographical locations of these sites, along with the corresponding number of harmonized Sentinel-2 and Landsat-8/9 scenes for experiments, are shown in Fig. 4. This figure also offers a comprehensive overview of the cloud percentages derived from cloud and cloud shadow flags of each scene in HLS datasets within the study periods.

Among the four study sites, Site 1 is situated in Assam, India, known for having one of the highest frequencies of flood occurrences globally (Rentschler et al., 2022). The selected flood event occurred between May and August 2022, extensively affecting Assam, India and the Sylhet region of Bangladesh. Site 2 is located in Sindh, Pakistan, which experienced a flood event in August and September 2022. This event was notable for its widespread impact, significant consequences, high satellite revisit frequency, and minimal cloud cover during the flooding, making it a focus for flood mapping study (Tulbure et al., 2022). Site 3 is located in Rio Grande do Sul, Brazil, which experienced a flood in October 2023 due to intense rainfall causing river overflow. This event featured heavy cloud cover, low satellite revisit frequency, and limited available observational information, marking its research significance. Site 4 is located in Michigan, USA, where a dam failure flood occurred on May 19, 2020. Unlike the other three events, the dam failure caused simultaneous expansion and shrinking of the water extent, making the reconstruction of cloud-covered water areas challenging.

3.2. Accuracy evaluation of the large foundation model for water extraction

The Prithvi-100M–Sen1Floods11 model (Jakubik et al., 2023), fine-tuned on the Sen1Floods11 dataset (Bonafilia et al., 2020), was used for water extraction in HLS images. Among the 446 labeled 512 × 512 chips in the Sen1Floods11 dataset, encompassing all 14 biomes and spanning 11 flood events, 267 chips were used for model fine-tuning, 89 chips for model validation, and the remaining 90 chips for model testing. The performance of the pre-trained model and the fine-tuned model for water extraction was evaluated in terms of five metrics, namely, overall accuracy (OA), precision, recall, mean intersect over union (mIoU), and F1-score. The accuracy comparison results are provided in Table 1. The results showed an increase of 1.08 % in precision and a decrease of 0.56 % in the recall, which resulted in an overall improvement of the fine-tuned model in OA with increased training epochs compared to the pre-trained model across test images in the Sen1Floods11 dataset. Note that the commission errors in water maps are more serious than the omission errors, as the latter can potentially be recovered during the reconstruction process of the proposed method, while the former might lead to more severe errors. In this case, the fine-tuned model is more appropriate than the pre-trained model. The 97.35 % OA indicates the promising capacity of the fine-tuned model for flood extent mapping.

3.3. Comparison of reconstructed flood maps and accuracy assessment

3.3.1. Time series flood extent mapping with the proposed reconstruction method

Fig. 5 shows typical seamless time series flood mapping results at four study sites generated by the proposed approach, and the complete flood mapping results are presented in Figs. S1–S4 as supplementary materials. False-color HLS images, initial water maps, and reconstructed flood maps are provided for each study site. From the false-color HLS images and initial water maps, the cloud cover during the flood period

Table 1
Accuracy comparison of pre-trained and fine-tuned models for water extraction with test images in the Sen1Floods11 dataset.

	OA	Precision	Recall	mIoU	F1-Score
Pre-trained model	97.25%	87.85%	**90.54%**	0.805	0.892
Fine-tuned model	**97.35%**	**88.93%**	89.98%	**0.809**	**0.895**

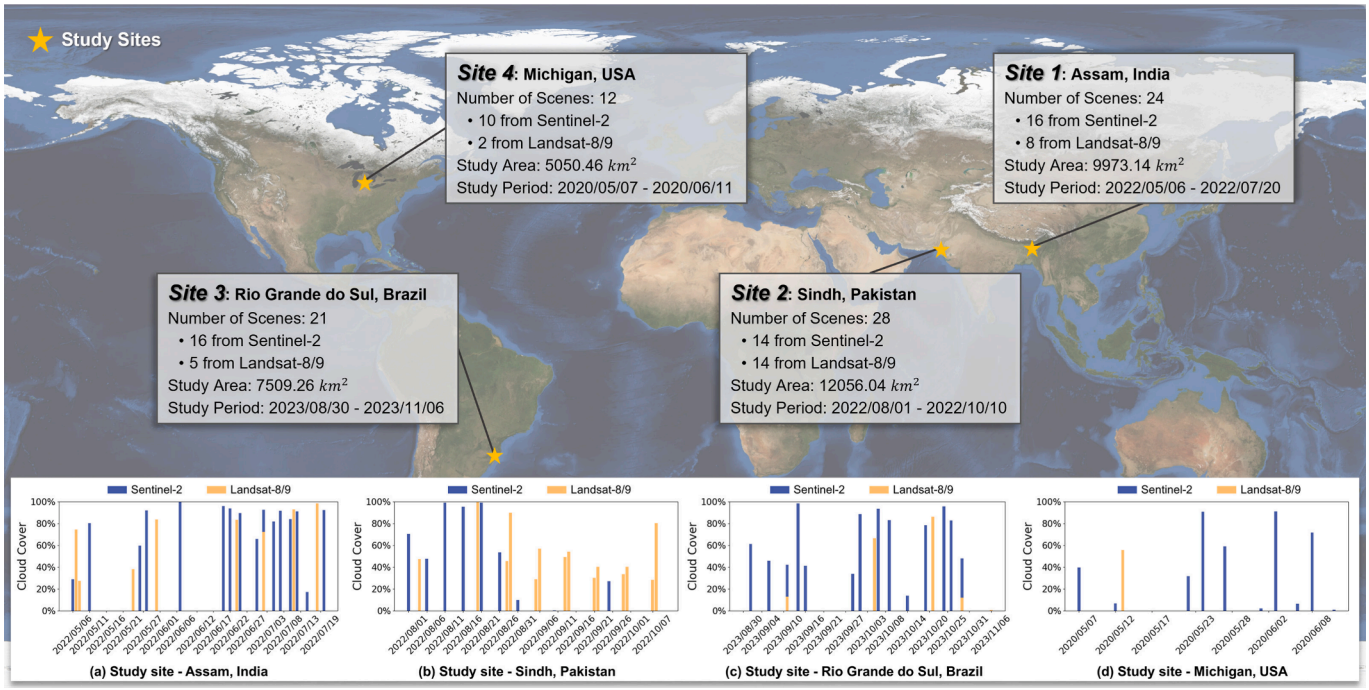

Fig. 4. Locations of four global study sites and cloud cover percentage distribution of HLS image time series for experiments (base map credit: NASA Visible Earth).

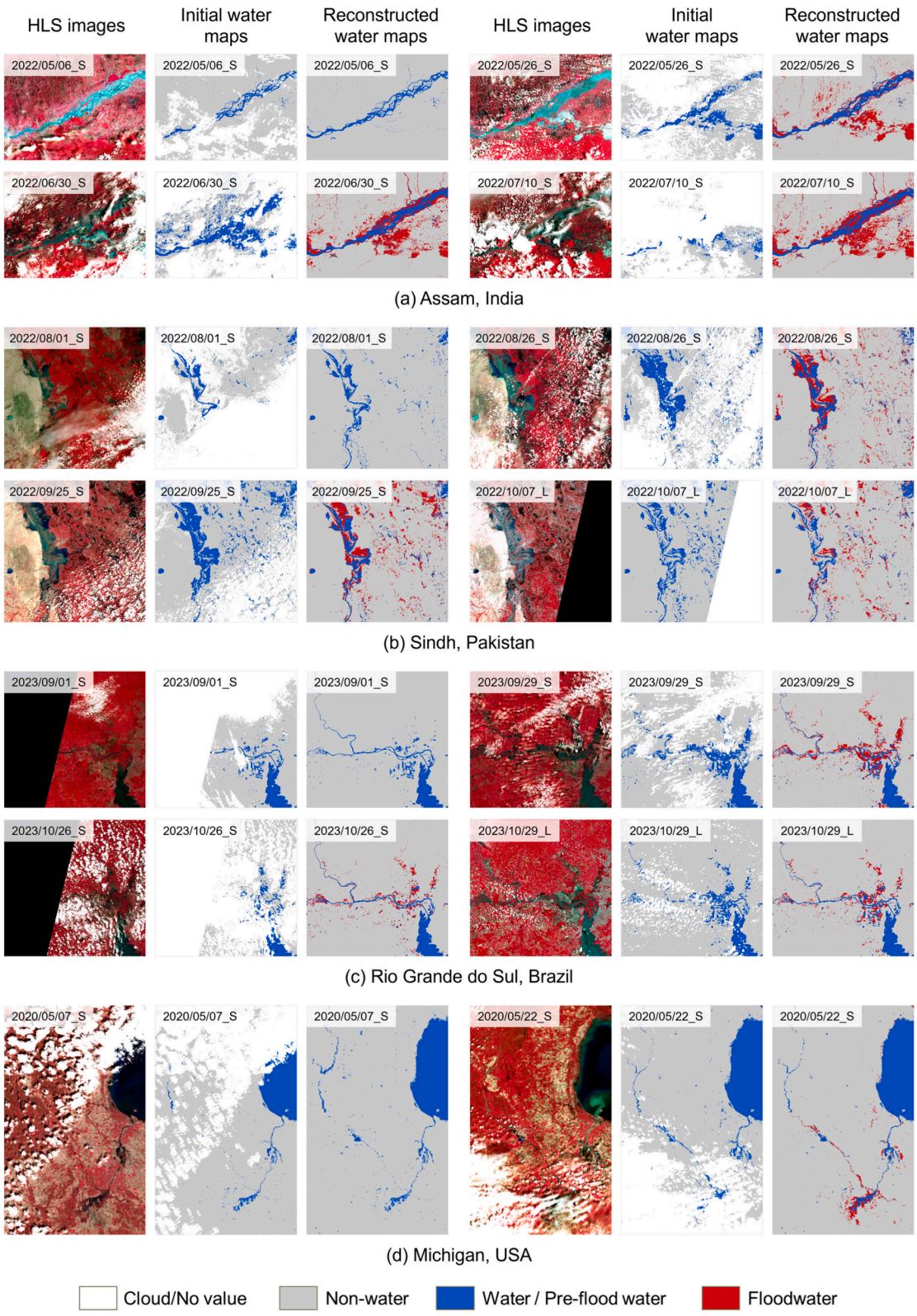

Fig. 5. Reconstruction results of the proposed method for seamless time series flood extent mapping. (a) Assam, India; (b) Sindh, Pakistan; (c) Rio Grande do Sul, Brazil; and (d) Michigan, USA. For each study site, 4 (for the first three sites) or 2 (for the last site) images acquired at different flood stages, and the corresponding water maps before and after reconstruction are selected to be shown as examples. The 1st and 4th columns show the original HLS images, the 2nd and 5th columns show the initial water maps overlaid with cloud/shadow masks, and the 3rd and 6th columns show the reconstructed water maps with flooded areas highlighted in red. Note that 'L' or 'S' follows the acquisition dates on each image to indicate that the HLS images were obtained from Landsat or Sentinel-2 satellites, respectively. (For interpretation of the references to colour in this figure legend, the reader is referred to the web version of this article.)

was significant, and valid flood observation data were sparse and limited. HLS images partly covering study areas were also used for experiments to enhance flood mapping frequency. As a result, the average satellite observation intervals for the four study sites were significantly improved from 8.3, 5.0, 6.2, and 4.4 days to 3.1, 2.5, 3.2, and 2.9 days, respectively. In no-value areas of these spatially incomplete images, the same reconstruction process as that in the cloud-covered areas was applied. The visual evaluation of the reconstructed flood maps suggested the effectiveness of the proposed method in seamless flood extent mapping under varying cloud conditions, i.e., in overall flood inundation trend and reconstruction details under different flood stages among the study sites.

In consideration of the connection between flood events and rainfall, comparing the areas of flood inundated regions with rainfall amounts could help generally evaluate the accuracy of the reconstructed flood maps. In this study, we collected daily precipitation data, i.e., CPC Global Unified Gauge-Based Analysis of Daily Precipitation from the NOAA Physical Sciences Laboratory website (https://psl.noaa.gov/), of each site during the study period. In Fig. 6, areas of identified pre-flood water and floodwater are compared with daily precipitation over the four study sites. Changes in flood inundated areas were not only related to daily precipitation over the study sites, but were also affected by topographic relief and the rainfall conditions nearby the study sites. Moreover, biases might exist in estimated change trends of floodwater areas because of the potential reconstruction error under varying cloud cover conditions. The comparison results showed a general consistency between the changes in floodwater areas and rainfall with consideration of the time lag effects, which demonstrated the effectiveness of the proposed method from a different perspective.

3.3.2. *Reconstruction performance evaluation under varying cloud cover conditions*

Simulation reconstruction experiments and comparative analysis were conducted to quantitatively evaluate the performance of the proposed method in the reconstruction of cloud-covered areas in water maps. This evaluation encompassed groups of simulation experiments in reconstructing cloud-covered areas and refining time series water maps, and comparisons of the reconstructed results of the proposed method with those of a gap-filling approach (Zhao and Gao, 2018). In this study, benchmark datasets with reference water maps were constructed to evaluate different reconstruction methods. We selected locally cloud-free HLS images with a size of approximately 1000 × 1000 pixels from each of the four study sites and manually annotated the extents of surface water. For the comprehensive evaluation of the performance of different methods in diverse scenarios, HLS images acquired at different flood stages (i.e., before/after flood, during flood) were involved to obtain reference water maps (i.e., ground truth) for comparison. In addition, real cloud masks with three levels of cloud coverage (i.e., low: <30 %, medium: 30–60 %, high: >60 %) were overlaid with reference water maps to simulate cloud-covered water maps for reconstruction. These real cloud masks were originally obtained from the QA band of collected HLS images and modified by applying morphological operations to determine the desired cloud cover percentages. Different methods were employed to reconstruct the simulated cloud-covered water maps together with other water maps in the time series of each study site. The reconstruction results of different methods were compared against reference water maps for quantitative accuracy evaluation, in which five metrics, namely, OA, precision, recall, mIoU, and F1-score, were adopted for accuracy measurement.

Fig. 7 shows the reconstruction results of the simulation experiments, and Table 2 provides the detailed accuracy evaluation results of the compared gap-filling method and the proposed method with and without the refinement process described in Section 2.3. The reconstruction results showed that our methods generally outperformed the compared gap-filling method in terms of OA, mIoU, and F1-score under different conditions, with much less water misidentification errors, as shown in Fig. 7, and such superiorities strengthened during flood. While the compared gap-filling method generally achieved higher recall

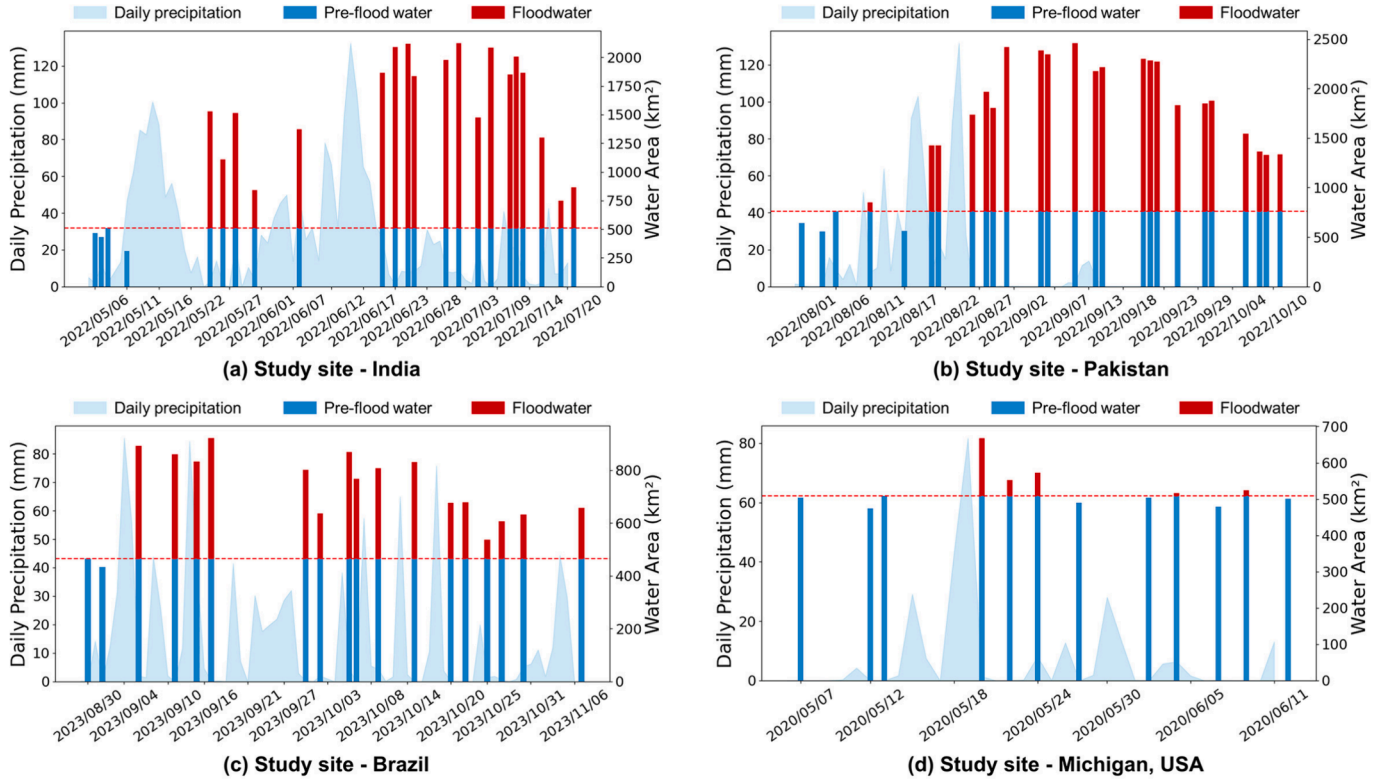

Fig. 6. Comparison of areas of identified floodwater (red bar) with daily precipitation (light blue background) over four test sites during flooding periods. (For interpretation of the references to colour in this figure legend, the reader is referred to the web version of this article.)

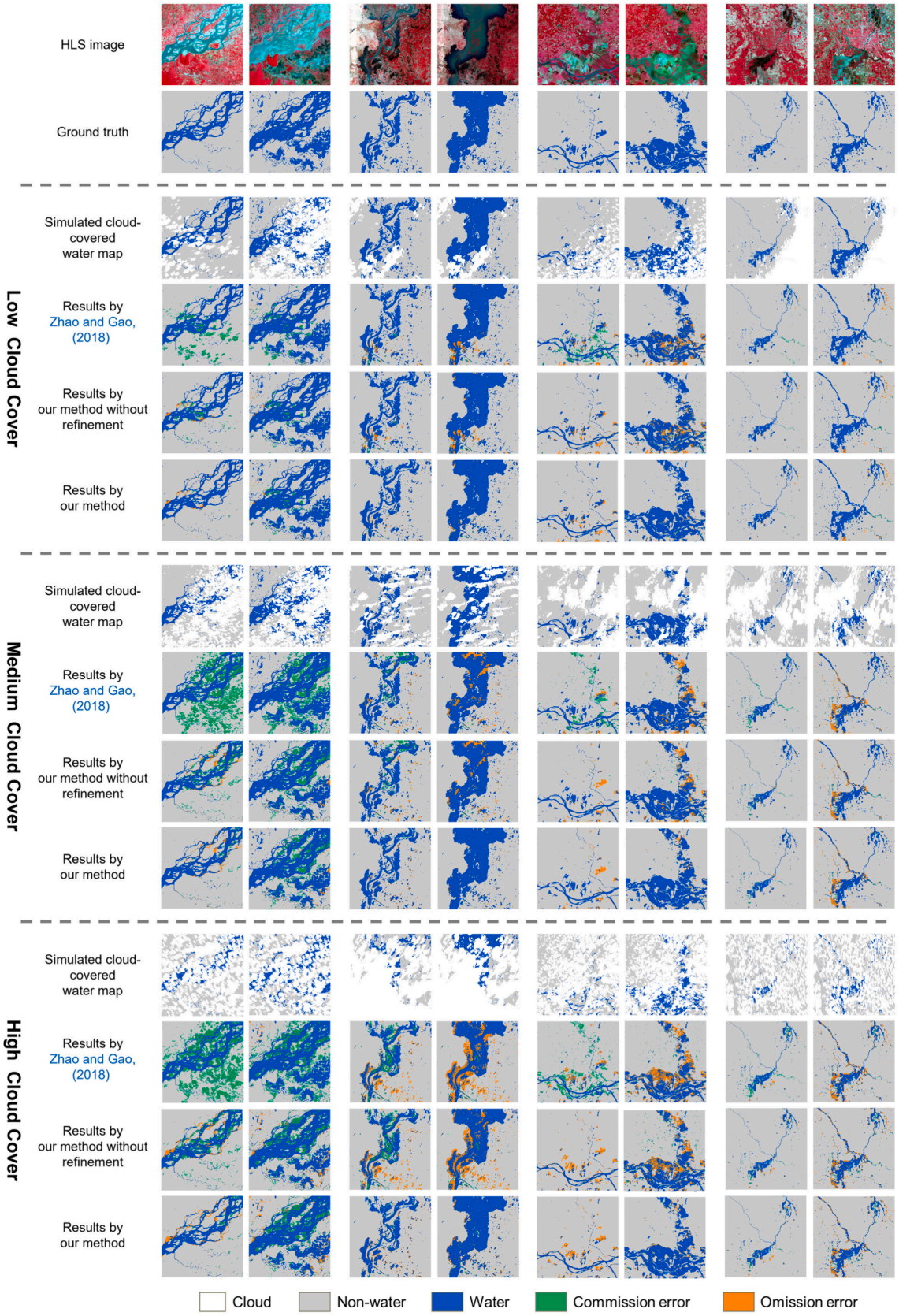

Fig. 7. Comparison of water extent maps reconstructed by the compared gap-filling method (Zhao and Gao, 2018) and the proposed method with and without spatiotemporal modeling-based refinement through simulated data experiments.

Table 2
Accuracy assessment of reconstructed water maps under varying cloud cover conditions before and during the flood events.

Phases	Cloud Cover	Method	OA	Precision	Recall	mIoU	F1-Score
During Floods	Low	Zhao and Gao (2018)	96.74 %	96.37 %	92.39 %	0.891	0.942
		Ours without refinement	97.29 %	96.79 %	93.22 %	0.904	0.949
		Ours	**98.50 %**	**97.49 %**	**96.50 %**	**0.942**	**0.970**
	Medium	Zhao and Gao (2018)	92.67 %	90.73 %	86.19 %	0.779	0.874
		Ours without refinement	94.56 %	92.56 %	87.83 %	0.816	0.898
		Ours	**96.14 %**	**93.57 %**	**91.96 %**	**0.864**	**0.924**
	High	Zhao and Gao (2018)	88.63 %	87.93 %	75.85 %	0.663	0.797
		Ours without refinement	91.08 %	89.61 %	78.76 %	0.714	0.833
		Ours	**94.75 %**	**91.84 %**	**88.57 %**	**0.822**	**0.898**
	Mean Acc.	Zhao and Gao (2018)	92.68 %	91.67 %	84.81 %	0.777	0.871
		Ours without refinement	94.31 %	92.99 %	86.60 %	0.811	0.893
		Ours	**96.46 %**	**94.30 %**	**92.34 %**	**0.876**	**0.931**
Before/After Floods	Low	Zhao and Gao (2018)	96.21 %	81.04 %	**94.41 %**	0.776	0.867
		Ours without refinement	98.35 %	95.39 %	90.86 %	0.868	0.928
		Ours	**98.79 %**	**97.71 %**	90.93 %	**0.890**	**0.940**
	Medium	Zhao and Gao (2018)	90.62 %	68.56 %	**94.10 %**	0.650	0.776
		Ours without refinement	96.39 %	87.42 %	88.72 %	0.782	0.877
		Ours	**98.07 %**	**94.43 %**	89.18 %	**0.845**	**0.915**
	High	Zhao and Gao (2018)	86.80 %	58.38 %	**85.58 %**	0.518	0.673
		Ours without refinement	93.71 %	81.45 %	76.37 %	0.635	0.775
		Ours	**96.87 %**	**92.10 %**	80.62 %	**0.747**	**0.853**
	Mean Acc.	Zhao and Gao (2018)	91.21 %	69.33 %	**91.36 %**	0.648	0.772
		Ours without refinement	96.15 %	88.09 %	85.32 %	0.762	0.860
		Ours	**97.91 %**	**94.75 %**	86.91 %	**0.828**	**0.903**

compared with our methods during non-flood periods, it sacrificed precision. Our method employed a stable ratio-based strategy to characterize water extent, making it less sensitive to the impact of varying cloud cover conditions. Furthermore, the locally asymptotic window reconstruction strategy employed in the proposed method considered the heterogeneity of local areas during flood, contributing to better reconstruction results.

Specifically, during flood and non-flood periods, the OA of the proposed method was 96.46 % and 97.91 %, respectively, showing absolute improvements of 3.78 % and 6.70 %, respectively, over the compared gap-filling method. The F1-score of the proposed method was 0.931 and 0.903, also showcasing obvious absolute increases of 0.060 and 0.131, respectively, compared with the gap-filling method. Under three conditions with low, medium, and high cloud coverage, the average F1-score of the proposed method was 0.955, 0.920, and 0.875, respectively. Although the reconstruction accuracy decreased as the cloud cover percentages increased, our method still demonstrated significant improvements in F1-score compared with the gap-filling method during flood and non-flood periods, with absolute increases of 0.051, 0.095, and 0.140 under low, medium, and high cloud coverage conditions, respectively. The above comparisons highlighted the effectiveness of the proposed method under different flood stages and varying cloud cover conditions. Furthermore, compared with the results of our method without refinement under low, medium, and high cloud coverage, our method with refinement showed absolute improvements of 0.016, 0.033, and 0.071 in terms of F1-score, respectively. This finding indicated that the time series refinement via spatiotemporal modeling played a more crucial role in the reconstruction of cloud-covered areas as cloud cover percentages increased, leading to greater accuracy improvements.

3.3.3. Comparison of reconstruction results with high-resolution PlanetScope images

Commercial PlanetScope satellite images with a high resolution of 3 m were introduced to further validate the reconstructed flood maps with real flood situations. PlanetScope satellites capture images of the entire Earth surface almost daily. In contrast with the 30 m-resolution HLS images, 3 m PlanetScope images allow for the identification of water with finer details, including smaller water bodies. We collected the PlanetScope images acquired at the same or nearest neighboring date as the HLS images over the four study sites. Due to the differences in imaging times of different satellites, cloud cover conditions and flooding extents in the HLS and PlanetScope images can vary substantially. Therefore, PlanetScope images can only be used for visual validation. Fig. 8 offers a visual comparison of the HLS images and the initial and reconstructed water maps with PlanetScope images and their derived Normalized Difference Vegetation Index (NDVI) maps. NDVI has been considered effective in distinguishing surface water from land pixels (Vermote and Saleous, 2007; Zhu and Woodcock, 2012), and is thus used to highlight the surface water in PlanetScope images. The comparison showed that the proposed method could achieve relatively accurate water map reconstruction even for images with limited cloud-free areas.

4. Discussion

4.1. Benefits of cloud reconstruction for flood mapping

To further demonstrate the significance and benefits of cloud reconstruction for flood mapping, we compared the differences between flood maps generated with and without cloud reconstruction. As illustrated in Fig. 9, the comparisons involved example HLS images taken during floods, the maximum water extents in the GSW dataset, and maximum water extents and flood duration maps composited with initial and reconstructed time series water maps. The initial water maps might be spatially incomplete owing to cloud cover. In this paper, the maximum water extent denotes the maximum-extent flood inundated areas, and the flood duration map represents the frequency (i.e., the duration of floods) at which inundation was observed. The results showed that the reconstructed maximum water extents provided timely flood information compared with the reference extents in the GSW dataset and more spatially complete flood inundated areas compared with those composited with initial water maps. Additionally, the reconstructed seamless water maps enhanced the spatial completeness of the composited flood duration maps in comparison with the flood duration maps composited with initial water maps. Similar conclusions on the benefits of cloud reconstruction for time series water mapping were discussed in recent studies (Bai et al., 2022; Huang et al., 2023). The maximum water extent and flood duration maps are crucial for flood monitoring and management, such as in flood impact assessments (Bofana et al., 2022). Although uncertainties may arise in the reconstruction, our method generally provides an effective way to generate

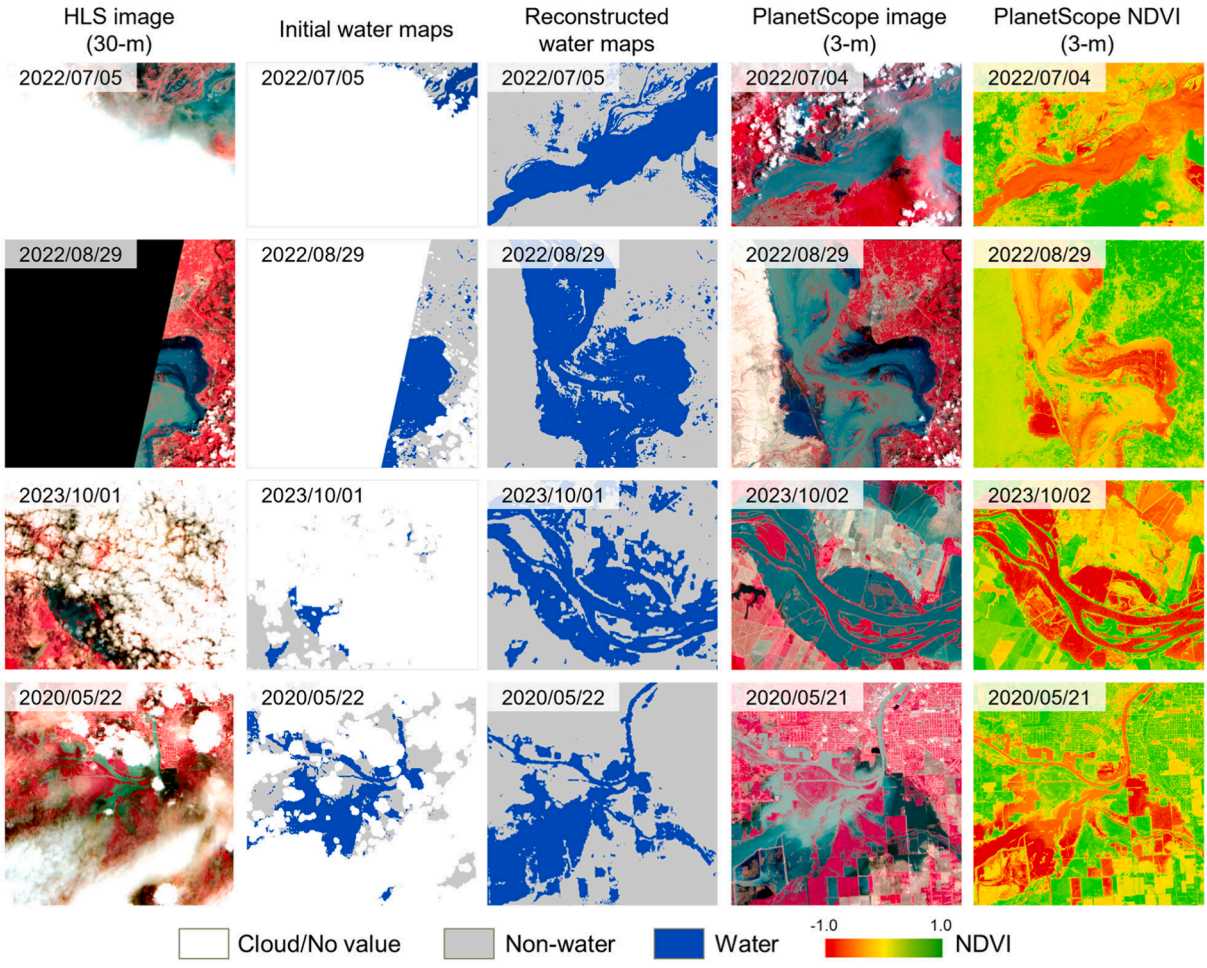

Fig. 8. Comparison of reconstructed flood extent maps with high-resolution PlanetScope images.

accurate and complete flood maps and thus benefits flood mapping under cloudy and rainy scenarios.

4.2. Incorporating SAR images for enhancement of flooding area reconstruction

All-weather SAR can penetrate clouds to conduct flood monitoring in all weather conditions; thus, SAR data are promising for delineating surface water under cloudy conditions. Theoretically, incorporating SAR data can enhance the temporal frequency of flood monitoring and provide spatially complete water maps. To validate the importance of SAR data in enhancing cloud-covered flooding area reconstruction, we collected Sentinel-1 SAR images within each study site from Google Earth Engine (GEE). Note that each Sentinel-1 image available on GEE was preprocessed with the Sentinel-1 toolbox, and the steps including noise removal, radiometric calibration, and terrain correction. Sentinel-1-derived water maps were obtained on the basis of the Sentinel-1 dual-polarized water index (Huang et al., 2023), which were then resampled and stacked with time series water maps derived from HLS images in a time order. The newly stacked time series maps were finally processed through time series refinement to reconstruct simulated cloud-covered water maps, as described in Section 3.3.2. We compared the accuracy evaluation results with and without incorporating Sentinel-1 images to assess the impact of SAR data on enhancing flood mapping. The experimental results showed that incorporating SAR data could enhance the reconstruction accuracy with a slight increase of 0.12 % in F1-score. However, as shown in Fig. 10, owing to the differences in imaging mechanisms between SAR and optical images, inconsistencies existed in the water extraction results derived from SAR and optical images (Markert et al., 2018), even when both were acquired on the same day. Thus, while incorporating SAR images is beneficial to enhance the flooding area reconstruction, especially under heavy cloud cover conditions, the harmonization of water maps derived from SAR and optical images warrants further exploration to strengthen this benefit.

4.3. Computational efficiency

Overall, the proposed method demonstrates high efficiency in processing time. Specifically, using one of the study areas in Assam, India, as an example, there are 24 HLS images in the time series, each with a size of 3849 × 2880 pixels and 76.10 % mean cloud cover. Tested on a desktop computer with an Intel i5-12490F CPU in a Python environment, our method took 9,234 s to complete the processing steps and generate the seamless time series flood maps. Note that the method by Zhao and Gao (2018) applied a global threshold for cloud reconstruction, allowing for a comprehensive comparison with our methods that apply global and local thresholds, respectively, in both efficiency and accuracy. Additionally, only the time cost for the cloud reconstruction step is considered among the methods. The efficiency assessment results show that the proposed method took 6,703 s with local reconstruction and 641 s with global reconstruction, as being compared to 482 s by the method of Zhao and Gao (2018). While our method, using a local sliding window strategy for local reconstruction, took longer than the method by Zhao and Gao (2018), which applied global reconstruction. Our method yields a significant improvement in mean overall accuracy, rising from 82.65 % to 92.76 % in Assam, India, as detailed in Section

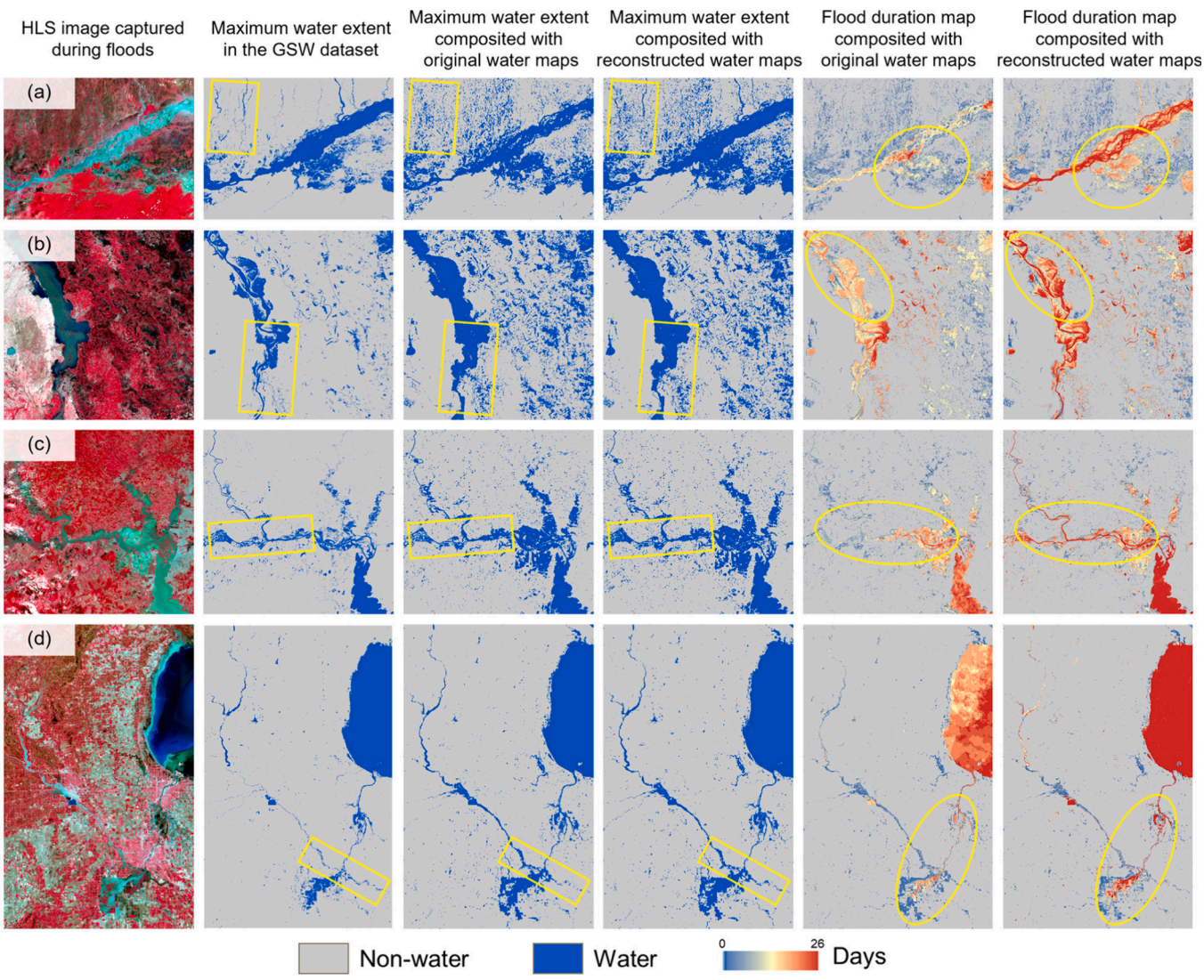

Fig. 9. Comparison of maximum water extent and flood duration maps composited with initial and reconstructed time series water maps. HLS images captured in (a) Assam, India on 2022/07/15; (b) Sindh, Pakistan on 2022/09/10; (c) Rio Grande do Sul, Brazil on 2023/09/11; (d) Michigan, USA on 2020/05/20. Yellow polygons in the figure panels highlight the major differences among the compared maps. (For interpretation of the references to colour in this figure legend, the reader is referred to the web version of this article.)

3.3.2. Nevertheless, the efficiency of our method could be further optimized through implementation enhancements and parallel processing.

4.4. Limitations of the study

Cloud cover significantly impairs the capabilities of optical satellites in monitoring floods. Although the reconstruction method proposed in this paper is effective in mitigating the influence of clouds to support continuous time series mapping of flood extent, limitations remained within its multiple steps.

The fine-tuned large foundation model exhibits high accuracy in water extraction, but it still introduces errors, such as misclassifying cloud shadows as surface water and omitting the surface water obstructed by vegetation, thus leaving room for improvements. Furthermore, the QA band of the HLS products tends to overestimate actual cloud cover, complicating the reconstruction process given the limited number of valid pixels. Therefore, developing an enhanced large foundation model with robust cloud masking capabilities is worthy of further exploration.

The performance of the proposed method decreases with the increase in percentages of cloud-covered areas that need to be reconstructed, especially under conditions of persistent and heavy cloud cover. Our assessments based on simulated data experiments indicate that for water map reconstruction, the method should be applied when the cloud cover is less than 96 % to maintain a typical F1-score accuracy above 0.8. When cloud cover exceeds 96 %, the results become considerably uncertain given insufficient cloud-free observational data. Therefore, a cloud cover percentage below 96 % is essential for effective water map reconstruction of cloud-covered areas.

Reconstructing cloud-covered areas in water maps during flood periods is more challenging compared with that during non-flood periods. The reason is that cloud cover is often more severe during flood periods than during non-flood periods, leading to a reduction in available temporally auxiliary information, thereby making the improvement through time series refinement less apparent. In addition, with the relatively low frequency of flooding in surface water dynamics, cloud-covered flooding area reconstruction is limited by the utilized water occurrence data, which might introduce omissions of floodwater in the reconstructed water maps, especially for extreme flooding events. While the time series refinement of water maps via spatiotemporal modeling is

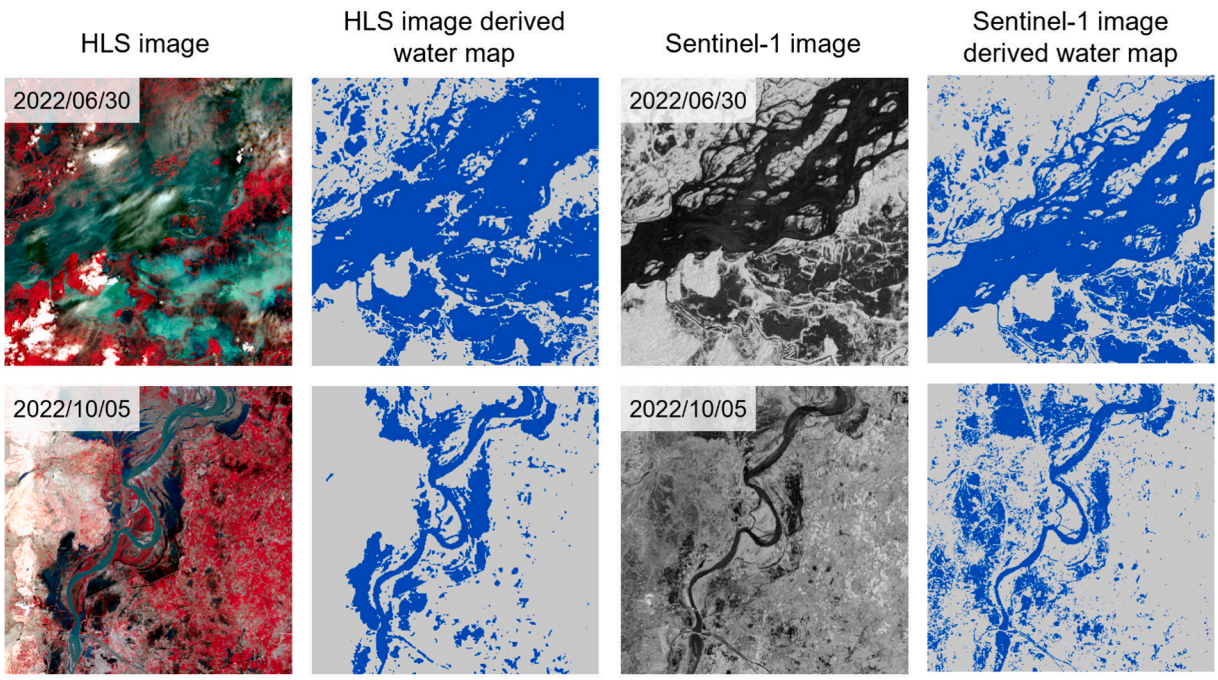

Fig. 10. Comparison of flood mapping results generated from optical (i.e., Landsat and Sentinel-2) and SAR (i.e., Sentinel-1) images acquired on the same day.

beneficial to alleviate this issue, such a limitation, sourced from water occurrence data, may hinder the potential of the proposed method in capturing extreme flood events intensified by climate change.

5. Conclusions

This study investigated seamless flood extent mapping using HLS image time series. We developed a robust method to reconstruct cloud-covered areas in time series water maps and evaluated its effectiveness for spatially continuous flood extent mapping under various flood scenarios with differing cloud cover conditions. The method was proven effective in enhancing time series flood monitoring and outperformed the compared gap-filling method in reconstructing cloud-covered flooding areas. Flood extent mapping experiments at four global study sites suggested an improvement in the average reconstruction accuracy, as measured by F1-score, from 0.871 to 0.931 during flood periods and from 0.772 to 0.903 during non-flood periods. The superiority of the proposed method became increasingly prominent as cloud cover increased, with an improvement in F1-score of up to 0.140 under high cloud coverage conditions.

The experimental results also indicated that reconstructing cloud-covered areas in time series water maps benefited the composition of maximum flood extent maps and flood duration maps. The reconstructed maps exhibited better spatial completeness and consistency compared with those composited without involving reconstruction. In addition, we consider the incorporation of SAR images as a promising way to enhance reconstruction results under persistent and dense cloud cover conditions, even though uncertainties and inconsistencies occurred between water maps derived from optical and SAR images owing to differences in their physical imaging mechanisms. The future combined use of optical and SAR images for flood monitoring should address this issue to ensure consistent flood extent mapping.

Overall, the proposed method provides an effective approach for flood monitoring under cloudy and rainy scenarios, thus supporting emergency response and disaster management. Future studies could explore the harmonization of water maps derived from multimodal and multisensor data. The delineation of water and cloud is crucial for effective flood monitoring, and the accuracy of water maps and cloud masks promises further enhancement with the introduction of a multi-temporal foundation model for image time series. Hydrodynamic modeling and additional auxiliary data, such as hydrodynamic simulation and accurate high-resolution DEM data, when available, can be utilized to refine reconstruction results further, especially when the proposed method is applied to mapping extreme flooding events.

CRediT authorship contribution statement

Zhiwei Li: Writing – original draft, Visualization, Validation, Software, Methodology, Investigation, Formal analysis, Data curation, Conceptualization. **Shaofen Xu:** Visualization, Validation, Software, Methodology, Investigation, Formal analysis, Data curation. **Qihao Weng:** Writing – review & editing, Supervision, Resources, Project administration, Funding acquisition, Formal analysis, Conceptualization.

Declaration of competing interest

The authors declare that they have no known competing financial interests or personal relationships that could have appeared to influence the work reported in this paper.

Acknowledgments

This research has received funding from the Global STEM Professorship (P0039329) and The Hong Kong Polytechnic University (P0046482, P0038446, and P0042484). This research was also partially supported by the National Natural Science Foundation of China (No. 42101357). The authors also acknowledge Planet Labs for providing high-resolution PlanetScope images that supported this study. Finally, the authors are grateful to the editors and reviewers for their constructive comments and suggestions, which helped improve the quality of this paper.

Appendix A. Supplementary data

Supplementary data to this article can be found online at https://doi.org/10.1016/j.isprsjprs.2024.07.022.

References

Bai, B., Tan, Y., Zhou, K., Donchyts, G., Haag, A., Weerts, A.H., 2022. Time-series surface water gap filling based on spatiotemporal neighbourhood similarity. Int. J. Appl. Earth Obs. Geoinf. 112, 102882 https://doi.org/10.1016/j.jag.2022.102882.

Bai, B., Tan, Y., Donchyts, G., Haag, A., Xu, B., Chen, G., Weerts, A.H., 2023. Naive Bayes classification-based surface water gap-filling from partially contaminated optical remote sensing image. J. Hydrol. 616 https://doi.org/10.1016/j.jhydrol.2022.128791.

Benoudjit, A., Guida, R., 2019. A novel fully automated mapping of the flood extent on sar images using a supervised classifier. Remote Sens. 11, 779. https://doi.org/10.3390/rs11070779.

Bentivoglio, R., Isufi, E., Jonkman, S.N., Taormina, R., 2022. Deep learning methods for flood mapping: a review of existing applications and future research directions. Hydrol. Earth Syst. Sci. 26, 4345–4378. https://doi.org/10.5194/hess-26-4345-2022.

Bofana, J., Zhang, M., Wu, B., Zeng, H., Nabil, M., Zhang, N., Elnashar, A., Tian, F., da Silva, J.M., Botão, A., Atumane, A., Mushore, T.D., Yan, N., 2022. How long did crops survive from floods caused by Cyclone Idai in Mozambique detected with multi-satellite data. Remote Sens. Environ. 269, 112808 https://doi.org/10.1016/j.rse.2021.112808.

Bonafilia, D., Tellman, B., Anderson, T., Issenberg, E., 2020. Sen1Floods11: A georeferenced dataset to train and test deep learning flood algorithms for sentinel-1, in: IEEE Computer Society Conference on Computer Vision and Pattern Recognition Workshops. IEEE, pp. 835–845. DOI: 10.1109/CVPRW50498.2020.00113.

Claverie, M., Ju, J., Masek, J.G., Dungan, J.L., Vermote, E.F., Roger, J.C., Skakun, S.V., Justice, C., 2018. The Harmonized Landsat and Sentinel-2 surface reflectance data set. Remote Sens. Environ. 219, 145–161. https://doi.org/10.1016/j.rse.2018.09.002.

Deng, Y., Jiang, W., Tang, Z., Li, J., Lv, J., Chen, Z., Jia, K., 2017. Spatio-temporal change of lake water extent in Wuhan urban agglomeration based on Landsat images from 1987 to 2015. Remote Sens. 9, 270. https://doi.org/10.3390/rs9030270.

DeVries, B., Huang, C., Armston, J., Huang, W., Jones, J.W., Lang, M.W., 2020. Rapid and robust monitoring of flood events using Sentinel-1 and Landsat data on the Google Earth Engine. Remote Sens. Environ. 240, 111664 https://doi.org/10.1016/j.rse.2020.111664.

Dosovitskiy, A., Beyer, L., Kolesnikov, A., Weissenborn, D., Zhai, X., Unterthiner, T., Dehghani, M., Minderer, M., Heigold, G., Gelly, S., Uszkoreit, J., Houlsby, N., 2021. An Image is Worth 16x16 Words: Transformers for Image Recognition at Scale. ICLR 2021 - 9th Int. Conf. Learn. Represent.

Feyisa, G.L., Meilby, H., Fensholt, R., Proud, S.R., 2014. Automated Water Extraction Index: A new technique for surface water mapping using Landsat imagery. Remote Sens. Environ. 140, 23–35. https://doi.org/10.1016/j.rse.2013.08.029.

Goffi, A., Stroppiana, D., Brivio, P.A., Bordogna, G., Boschetti, M., 2020. Towards an automated approach to map flooded areas from Sentinel-2 MSI data and soft integration of water spectral features. Int. J. Appl. Earth Obs. Geoinf. 84, 101951 https://doi.org/10.1016/j.jag.2019.101951.

He, K., Chen, X., Xie, S., Li, Y., Dollar, P., Girshick, R., 2022. Masked Autoencoders Are Scalable Vision Learners, in: Proceedings of the IEEE Computer Society Conference on Computer Vision and Pattern Recognition. pp. 15979–15988. DOI: 10.1109/CVPR52688.2022.01553.

He, Y., Wang, J., Zhang, Y., Liao, C., 2024. An efficient urban flood mapping framework towards disaster response driven by weakly supervised semantic segmentation with decoupled training samples. ISPRS J. Photogramm. Remote Sens. 207, 338–358. https://doi.org/10.1016/j.isprsjprs.2023.12.009.

Huang, M., Jin, S., 2020. Rapid flood mapping and evaluation with a supervised classifier and change detection in Shouguang using Sentinel-1 SAR and Sentinel-2 optical data. Remote Sens. 12, 2073. https://doi.org/10.3390/rs12132073.

Huang, W., Wang, F., Duan, W., Tang, L., Qin, J., Meng, X., 2023. Image similarity-based gap filling method can effectively enrich surface water mapping information. ISPRS J. Photogramm. Remote Sens. 202, 528–544. https://doi.org/10.1016/j.isprsjprs.2023.07.011.

Ipcc, 2023. Climate Change 2021 – The Physical Science Basis. Cambridge University Press. https://doi.org/10.1017/9781009157896.

Jakubik, J., Chu, L., Fraccaro, P., Gomes, C., Nyirjesy, G., Bangalore, R., Lambhate, D., Das, K., Oliveira Borges, D., Kimura, D., Simumba, N., Szwarcman, D., Muszynski, M., Weldemariam, K., Zadrozny, B., Ganti, R., Costa, C., Edwards Blair & Watson, C., Mukkavilli, K., Schmude Johannes & Hamann, H., Robert, P., Roy, S., Phillips, C., Ankur, K., Ramasubramanian, M., Gurung, I., Leong, W.J., Avery, R., Ramachandran, R., Maskey, M., Olofossen, P., Fancher, E., Lee, T., Murphy, K., Duffy, D., Little, M., Alemohammad, H., Cecil, M., Li, S., Khallaghi, S., Godwin, D., Ahmadi, M., Kordi, F., Saux, B., Pastick, N., Doucette, P., Fleckenstein, R., Luanga, D., Corvin, A., Granger, E., 2023. Prithvi-100M.https://github.com/NASA-IMPACT/hls-foundation-os. DOI: 10.57967/hf/0952.

Kasetkasem, T., Phuhinkong, P., Rakwatin, P., Chanwimaluang, T., Kumazawa, I., 2014. A flood mapping algorithm from cloud contaminated MODIS time-series data using a Markov random field model. Int. Geosci. Remote Sens. Symp. 2507–2510 https://doi.org/10.1109/IGARSS.2014.6946982.

Konapala, G., Kumar, S.V., Khalique Ahmad, S., 2021. Exploring Sentinel-1 and Sentinel-2 diversity for flood inundation mapping using deep learning. ISPRS J. Photogramm. Remote Sens. 180, 163–173. https://doi.org/10.1016/j.isprsjprs.2021.08.016.

Li, S.Z., 2009. Markov Random Field Modeling in Image Analysis. Springer Science & Business Media.

Li, X., Ling, F., Cai, X., Ge, Y., Li, X., Yin, Z., Shang, C., Jia, X., Du, Y., 2021. Mapping water bodies under cloud cover using remotely sensed optical images and a spatiotemporal dependence model. Int. J. Appl. Earth Obs. Geoinf. 103, 102470 https://doi.org/10.1016/j.jag.2021.102470.

Li, M., Lu, S., Du, C., Wang, Y., Fang, C., Li, X., Tang, H., Baig, M.H.A., Ikhumhen, H.O., 2022a. Time-series surface water reconstruction method (TSWR) based on spatial distance relationship of multi-stage water boundaries. Int. J. Digit. Earth 15, 2335–2354. https://doi.org/10.1080/17538947.2022.2159553.

Li, J., Narayanan, R.M., 2003. A Shape-Based Approach to Change Detection of Lakes Using Time Series Remote Sensing Images. IEEE Trans. Geosci. Remote Sens. 41, 2466–2477. https://doi.org/10.1109/TGRS.2003.817267.

Li, Z., Shen, H., Weng, Q., Zhang, Y., Dou, P., Zhang, L., 2022c. Cloud and cloud shadow detection for optical satellite imagery: Features, algorithms, validation, and prospects. ISPRS J. Photogramm. Remote Sens. 188, 89–108. https://doi.org/10.1016/j.isprsjprs.2022.03.020.

Li, S., Sun, D., Goldberg, M.D., Kalluri, S., Sjoberg, B., Lindsey, D., Hoffman, J.P., DeWeese, M., Connelly, B., Mckee, P., Lander, K., 2022b. A downscaling model for derivation of 3-D flood products from VIIRS imagery and SRTM/DEM. ISPRS J. Photogramm. Remote Sens. 192, 279–298. https://doi.org/10.1016/j.isprsjprs.2022.08.025.

Li, Z., Weng, Q., Zhou, Y., Dou, P., Ding, X., 2024. Learning spectral-indices-fused deep models for time-series land use and land cover mapping in cloud-prone areas: The case of Pearl River Delta. Remote Sens. Environ. 308, 114190 https://doi.org/10.1016/j.rse.2024.114190.

Liang, J., Liu, D., 2020. A local thresholding approach to flood water delineation using Sentinel-1 SAR imagery. ISPRS J. Photogramm. Remote Sens. 159, 53–62. https://doi.org/10.1016/j.isprsjprs.2019.10.017.

Liu, F., Chen, D., Guan, Z., Zhou, X., Zhu, J., Ye, Q., Fu, L., Zhou, J., 2023. RemoteCLIP: A Vision Language Foundation Model for Remote Sensing. IEEE Trans. Geosci. Remote Sens. https://doi.org/10.1109/TGRS.2024.3390838.

Markert, K.N., Chishtie, F., Anderson, E.R., Saah, D., Griffin, R.E., 2018. On the merging of optical and SAR satellite imagery for surface water mapping applications. Results Phys. 9, 275–277. https://doi.org/10.1016/j.rinp.2018.02.054.

McCormack, T., Campanyà, J., Naughton, O., 2022. A methodology for mapping annual flood extent using multi-temporal Sentinel-1 imagery. Remote Sens. Environ. 282, 113273 https://doi.org/10.1016/j.rse.2022.113273.

McFeeters, S.K., 1996. The use of the Normalized Difference Water Index (NDWI) in the delineation of open water features. Int. J. Remote Sens. 17, 1425–1432. https://doi.org/10.1080/01431169608948714.

Moussouris, J., 1974. Gibbs and Markov random systems with constraints. J. Stat. Phys. 10, 11–33. https://doi.org/10.1007/BF01011714.

Mullen, C., Penny, G., Müller, M.F., 2021. A simple cloud-filling approach for remote sensing water cover assessments. Hydrol. Earth Syst. Sci. 25, 2373–2386. https://doi.org/10.5194/hess-25-2373-2021.

Notti, D., Giordan, D., Caló, F., Pepe, A., Zucca, F., Galve, J.P., 2018. Potential and limitations of open satellite data for flood mapping. Remote Sens. 10, 1673. https://doi.org/10.3390/rs10111673.

Pekel, J.-F., Cottam, A., Gorelick, N., Belward, A.S., 2016. High-resolution mapping of global surface water and its long-term changes. Nature 540, 418–422. https://doi.org/10.1038/nature20584.

Psomiadis, E., Diakakis, M., Soulis, K.X., 2020. Combining SAR and optical earth observation with hydraulic simulation for flood mapping and impact assessment. Remote Sens. 12, 1–29. https://doi.org/10.3390/rs12233980.

Rentschler, J., Salhab, M., Jafino, B.A., 2022. Flood exposure and poverty in 188 countries. Nat. Commun. 13 https://doi.org/10.1038/s41467-022-30727-4.

Shastry, A., Carter, E., Coltin, B., Sleeter, R., McMichael, S., Eggleston, J., 2023. Mapping floods from remote sensing data and quantifying the effects of surface obstruction by clouds and vegetation. Remote Sens. Environ. 291, 113556 https://doi.org/10.1016/j.rse.2023.113556.

Shen, H., Li, X., Cheng, Q., Zeng, C., Yang, G., Li, H., Zhang, L., 2015. Missing Information Reconstruction of Remote Sensing Data: A Technical Review. IEEE Geosci. Remote Sens. Mag. 3, 61–85. https://doi.org/10.1109/MGRS.2015.2441912.

Sun, X., Li, L., Zhang, B., Chen, D., Gao, L., 2015. Soft urban water cover extraction using mixed training samples and support vector machines. Int. J. Remote Sens. 36, 3331–3344.

Sun, F., Zhao, Y., Gong, P., Ma, R., Dai, Y., 2014. Monitoring dynamic changes of global land cover types: fluctuations of major lakes in China every 8 days during 2000–2010. Chinese Sci. Bull. 59, 171–189. https://doi.org/10.1007/s11434-013-0045-0.

Tellman, B., Sullivan, J.A., Kuhn, C., Kettner, A.J., Doyle, C.S., Brakenridge, G.R., Erickson, T.A., Slayback, D.A., 2021. Satellite imaging reveals increased proportion of population exposed to floods. Nature 596, 80–86. https://doi.org/10.1038/s41586-021-03695-w.

Tulbure, M.G., Broich, M., Perin, V., Gaines, M., Ju, J., Stehman, S.V., Pavelsky, T., Masek, J.G., Yin, S., Mai, J., Betbeder-Matibet, L., 2022. Can we detect more ephemeral floods with higher density harmonized Landsat Sentinel 2 data compared to Landsat 8 alone? ISPRS J. Photogramm. Remote Sens. 185, 232–246. https://doi.org/10.1016/j.isprsjprs.2022.01.021.

Valman, S.J., Boyd, D.S., Carbonneau, P.E., Johnson, M.F., Dugdale, S.J., 2024. An AI approach to operationalise global daily PlanetScope satellite imagery for river water masking. Remote Sens. Environ. 301, 113932 https://doi.org/10.1016/j.rse.2023.113932.

Vaswani, A., Shazeer, N., Parmar, N., Uszkoreit, J., Jones, L., Gomez, A.N., Kaiser, Ł., Polosukhin, I., 2017. Attention is all you need. Adv. Neural Informat. Process. Syst. 5999–6009.

Vermote, E., Saleous, N., 2007. LEDAPS surface reflectance product description. Coll. Park Univ. 1–21.

Wang, C., Jia, M., Chen, N., Wang, W., 2018. Long-term surface water dynamics analysis based on landsat imagery and the Google Earth Engine Platform: A case study in the middle Yangtze River Basin. Remote Sens. 10, 1635. https://doi.org/10.3390/rs10101635.

Wang, Y., Li, Z., Zeng, C., Xia, G.S., Shen, H., 2020. An urban water extraction method combining deep learning and google earth engine. IEEE J. Sel. Top. Appl. Earth Obs. Remote Sens. https://doi.org/10.1109/JSTARS.2020.2971783.

Wang, D., Zhang, Q., Xu, Y., Zhang, J., Du, B., Tao, D., Zhang, L., 2023. Advancing plain vision transformer toward remote sensing foundation model. IEEE Trans. Geosci. Remote Sens. 61, 1–15. https://doi.org/10.1109/TGRS.2022.3222818.

Xu, H., 2005. A study on information extraction of water body with the modified normalized difference water index (MNDWI). Natl. Remote Sens. Bull. 589–595. https://doi.org/10.11834/jrs.20050586.

Yang, X., Qin, Q., Yésou, H., Ledauphin, T., Koehl, M., Grussenmeyer, P., Zhu, Z., 2020. Monthly estimation of the surface water extent in France at a 10-m resolution using Sentinel-2 data. Remote Sens. Environ. 244, 111803 https://doi.org/10.1016/j.rse.2020.111803.

Zeng, Z., Gan, Y., Kettner, A.J., Yang, Q., Zeng, C., Brakenridge, G.R., Hong, Y., 2020. Towards high resolution flood monitoring: An integrated methodology using passive microwave brightness temperatures and Sentinel synthetic aperture radar imagery. J. Hydrol. 582, 124377 https://doi.org/10.1016/j.jhydrol.2019.124377.

Zhang, Q., Yuan, Q., Li, Z., Sun, F., Zhang, L., 2021. Combined deep prior with low-rank tensor SVD for thick cloud removal in multitemporal images. ISPRS J. Photogramm. Remote Sens. 177, 161–173. https://doi.org/10.1016/j.isprsjprs.2021.04.021.

Zhao, G., Gao, H., 2018. Automatic correction of contaminated images for assessment of reservoir surface area dynamics. Geophys. Res. Lett. 45, 6092–6099. https://doi.org/10.1029/2018GL078343.

Zhu, Z., Wang, S., Woodcock, C.E., 2015. Improvement and expansion of the Fmask algorithm: Cloud, cloud shadow, and snow detection for Landsats 4–7, 8, and Sentinel 2 images. Remote Sens. Environ. 159, 269–277. https://doi.org/10.1016/j.rse.2014.12.014.

Zhu, Z., Woodcock, C.E., 2012. Object-based cloud and cloud shadow detection in Landsat imagery. Remote Sens. Environ. 118, 83–94. https://doi.org/10.1016/j.rse.2011.10.028.